Experimental and theoretical investigation of $Cr_{1-x}Sc_xN$ solid solutions for thermoelectrics

Kerdsongpanya, Sit; Sun, Bo ; Eriksson, Fredrik ; Jensen, Jens; Lu, Jun; Koh, Yee Kan ; Van Nong, Ngo; Balke, Benjamin; Alling, Björn ; Eklund, Per

Published in:
Journal of Applied Physics

Link to article, DOI:
10.1063/1.4968570

Publication date:
2016

Document Version
Publisher's PDF, also known as Version of record

AIP Journal of Applied Physics

Experimental and theoretical investigation of Cr1-xScxN solid solutions for thermoelectrics

Sit Kerdsongpanya, Bo Sun, Fredrik Eriksson, Jens Jensen, Jun Lu, Yee Kan Koh, Ngo Van Nong, Benjamin Balke, Björn Alling, and Per Eklund

Citation: Journal of Applied Physics **120**, 215103 (2016); doi: 10.1063/1.4968570
View online: http://dx.doi.org/10.1063/1.4968570
View Table of Contents: http://scitation.aip.org/content/aip/journal/jap/120/21?ver=pdfcov
Published by the AIP Publishing

Experimental and theoretical investigation of $Cr_{1-x}Sc_xN$ solid solutions for thermoelectrics

Sit Kerdsongpanya,[1,2,a)] Bo Sun,[3] Fredrik Eriksson,[1] Jens Jensen,[1] Jun Lu,[1] Yee Kan Koh,[3] Ngo Van Nong,[4] Benjamin Balke,[5] Björn Alling,[1,6] and Per Eklund[1,a)]

[1]*Thin Film Physics Division, Department of Physics, Chemistry, and Biology (IFM), Linköping University, SE-581 83 Linköping, Sweden*

[2]*Department of Materials Science and Engineering, Rensselaer Polytechnic Institute, Troy, New York 12180, USA*

[3]*Department of Mechanical Engineering, National University of Singapore, Block EA, 9 Engineering Drive 1, #07-08, Singapore 117576*

[4]*Department of Energy Conversion and Storage, Technical University of Denmark, Risø Campus, Frederiksborgvej 399, Building 779, 4000 Roskilde, Denmark*

[5]*Institute of Inorganic and Analytical Chemistry, Johannes Gutenberg University, D-55131 Mainz, Germany*

[6]*Max-Planck-Institut für Eisenforschung GmbH, D-40237 Düsseldorf, Germany*

(Received 15 August 2016; accepted 10 November 2016; published online 1 December 2016)

The ScN- and CrN-based transition-metal nitrides have recently emerged as a novel and unexpected class of materials for thermoelectrics. These materials constitute well-defined model systems for investigating mixing thermodynamics, phase stability, and band structure aiming for property tailoring. Here, we demonstrate an approach to tailor their thermoelectric properties by solid solutions. The trends in mixing thermodynamics and densities-of-states (DOS) of rocksalt-$Cr_{1-x}Sc_xN$ solid solutions ($0 \le x \le 1$) are investigated by first-principles calculations, and $Cr_{1-x}Sc_xN$ thin films are synthesized by magnetron sputtering. Pure CrN exhibits a high power factor, 1.7×10^{-3} W m^{-1} K^{-2} at 720 K, enabled by a high electron concentration thermally activated from N vacancies. Disordered rocksalt-$Cr_{1-x}Sc_xN$ solid solutions are thermodynamically stable, and calculated DOS suggest the possibility for power-factor improvement by Sc*3d* orbital delocalization on Cr*3d* electrons giving decreasing electrical resistivity, while localized Cr*3d* orbitals with a large DOS slope may yield an improved Seebeck coefficient. Sc-rich solid solutions show a large improvement in power factor compared to pure ScN, and all films have power factors above that expected from the rule-of-mixture. These results corroborate the theoretical predictions and enable tailoring and understanding of structure-transport-property correlations of $Cr_{1-x}Sc_xN$. *Published by AIP Publishing.*
[http://dx.doi.org/10.1063/1.4968570]

I. INTRODUCTION

The increasing demand for renewable clean energy pushes the research community to find new energy technologies. Thermoelectric devices have the ability to convert heat (temperature gradients) into electricity or vice versa without any moving parts or intermediate cooling/heating agents.[1] The source of the temperature gradient can be natural heat from geothermal or solar energy, or waste heat in automobiles or industries, making thermoelectrics an attractive technology for energy harvesting. The conversion efficiency of a thermoelectric device directly depends on the temperature gradient across the device and a material-dependent dimensionless parameter called the thermoelectric figure of merit ZT, defined as $ZT = S^2T/\rho\kappa$, where S is the Seebeck coefficient, ρ is the electrical resistivity, κ is the sum of electrical and lattice thermal conductivities, $\kappa = \kappa_{el} + \kappa_{ph}$, and T is the average temperature between the hot and the cold side.[2] Since S, ρ, and κ are interdependent, it is difficult to increase ZT. Therefore, one must consider materials with both high ZT and high thermal stability.

Following these requirements, transition-metal nitrides become interesting materials to consider for thermoelectric applications in harsh environments because of their excellent mechanical and electrical properties with high thermal and chemical stability.[3] Among the transition-metal nitrides, CrN and ScN show a range of suitable properties. CrN exhibits high hardness, wear resistance, and corrosion resistance,[4–8] and can furthermore easily be synthesized in bulk,[9–11] as thin films, or thick coatings (100 nm–100 μm).[12–14] On the other hand, ScN has both high temperature stability and high hardness, $H \sim 21$ GPa.[15–17] In terms of thermoelectric properties, CrN has a high Seebeck coefficient of $-135\ \mu$V/K (Refs. 18–20) and quite low thermal conductivity of 1.76 W m^{-1} K^{-1} at room temperature.[18,19] However, CrN has the drawback of a relatively high electrical resistivity in the range of 2×10^{-4} to 1×10^{-3} Ωm at room temperature.[4,14,18–21] This is because the localized *3d* orbitals in CrN give a large effective mass for electrons resulting in large Seebeck coefficient, but high electrical resistivity.[22–24] ScN is a narrow-bandgap semiconductor, but can in thin-film form exhibit low, metallic-like, electrical resistivity of about 1.0×10^{-6} to 2.2×10^{-6} Ωm with a relatively large Seebeck coefficient of about $-75\ \mu$V/K at room temperature.[25–27] A weakness of ScN is its rather high thermal conductivity of 10 W m^{-1} K^{-1}.

a)Authors to whom correspondence should be addressed. Electronic addresses: kerdss@rpi.edu and perek@ifm.liu.se

This background on CrN and ScN presents a possible approach to improve their thermoelectric properties by forming a solid solution.[28] The hypothesis is that the characteristic empty *3d* orbitals in Sc could yield a decrease in the electrical resistivity of CrN by delocalizing the electrons in Cr *3d* orbitals, and a possibility to increase Seebeck coefficient in ScN by filling empty *3d* orbitals in ScN with localized Cr *3d* orbitals. Furthermore, one can expect a decrease in thermal conductivity of ScN and CrN due to alloying-element phonon scattering. In this study, we report theoretical investigations of phase stability and the electronic density of states in $Cr_{1-x}Sc_xN$, and experimental determination of thermoelectric properties of disordered $Cr_{1-x}Sc_xN$ solid solutions.

II. COMPUTATIONAL AND EXPERIMENTAL DETAILS

A. Calculations of mixing thermodynamic and electric density of states

All calculations in this work were performed based on first-principles density functional theory (DFT) using the Kohn-Sham equations[29] with Projector Augmented Wave method (PAW)[30] as implemented in the Vienna *Ab-initio* Simulation Package (VASP) code.[31,32] The local density approximation with a Hubbard Coulomb term (LDA+U) was used as exchange-correlation energy.[33,34] We use the value of 3 eV for the effective $U^{eff} = U - J$ (U^{eff} is designated as U elsewhere in the paper) applied on to *3d* orbitals. This value was found to be optimal in the CrN system for reproducing both the experimental lattice parameter of the paramagnetic cubic phase, the experimental degree of orthorhombic distortion in the antiferromagnetic phase, and the experimental valence band electronic structure of the cubic phase.[35] Also other groups have reached similar conclusions regarding the U-value for CrN.[23,24] Moreover, we performed test calculations of effective U in Sc *3d* orbitals; the results show that the calculated lattice constant for pure ScN using LDA+U with the same U = 3 eV closely match the experimental lattice constant also for this nitride. Therefore, we used a consistent U = 3 eV applied to 3d orbitals in both Cr and Sc in all systems.

To determine the phase stability of the rock salt (B1) structure alloys in the $Cr_{1-x}Sc_xN$ solid solution system, we calculated the mixing enthalpy from the calculated formation energy of the pure binary nitrides CrN and ScN at zero pressure, that is, using the total energy at the optimal volume for each specific concentration. In order to capture the paramagnetic states in CrN and $Cr_{1-x}Sc_xN$ system, we also set the initial magnetic moments of Cr atoms in equal number to either 3 or −3 Bohr magnetons. The special quasirandom structures (SQSs)-based approach[36] was used to generate substitutionally disordered 3-metal-component solid solutions on the rock salt (B1) lattice$(Cr^{\uparrow}_{0.5}Cr^{\downarrow}_{0.5})_{1-x}Sc_xN$ with the compositions x = 0.25, 0.50, and 0.75. For pure CrN a two-component SQS was used for modelling $Cr^{\uparrow}_{0.5}Cr^{\downarrow}_{0.5}N$. We used for all SQS a $4 \times 4 \times 4$ repetitions of the face-centered-cubic (fcc) unit cell consisting of 64 atoms on each sublattice (i.e., 128 atom supercells) to obtain converged total energies. The pair correlation functions, quantifying the configurational state of a structure,[37,38] were for these SQS structures identical to the ideal disordered system on the first two nearest neighbor shell and differing with less than 0.04 on the first seven shells for all compositions. We also considered chemically ordered, but magnetically disordered configurations which are represented by the B1-$L1_1$ (CuPt) metal-sublattice ordering with composition x = 0.50. This structure was selected since it represents the maximum ordering possible on the second metal coordination shell on the fcc lattice. In the B1 nitrides, the nitrogen atom is placed in the octahedral site in between two second-neighbor metals. Strong lattice relaxations tend to favor to have two different types of metals on this coordination shell. Thus, this B1-$L1_1$ structure, predicted as the lowest energy ordering in $Ti_{0.5}Mg_{0.5}N$ (Ref. 39) and $Zr_{0.5}Gd_{0.5}N$ (Ref. 40) contrast strongly to the phase-separated state and together with clustering and the SQS structure give a good estimate of the energy span of different configurations with the composition x = 0.50. To get a guideline for the effect of temperature on phase stability, we consider the change in Gibbs free energy of the disordered solid solutions

$$\Delta G(x,T) = \Delta H_{mix}(x) - T\Delta S_{mix}(x), \quad (1)$$

where $\Delta H(x)$ is the mixing enthalpy per formula unit which is calculated by

$$\Delta H_{mix}(x) = H_{(Cr_{1-x}Sc_xN)} - (1-x)H_{CrN} - xH_{ScN}, \quad (2)$$

where the enthalpies are considered at zero pressure as the energies of each phase is taken at its corresponding equilibrium volume. The mixing entropy $\Delta S(x)$ can be estimated from the mean-field approximation

$$S_{mf} = -k_B\{x\ln(x) + (1-x)\ln(1-x)\}, \quad (3)$$

where x is the fraction of considered solid solution material. This formula is a simplification of the real entropy and is used to estimate the effect of temperature on phase stability. In this study, the vibrational contributions are neglected because they are not of critical importance for the ability to draw qualitative conclusions about mixing trends far below the melting point of these nitrides, which are as high as above 2000 K.[3] A plane wave cut-off of 400 eV was used. A Monkhorst-Pack[41] k-point mesh of $7 \times 7 \times 7$ points for 128 cells and $21 \times 21 \times 21$ points for the binary ScN was used. In all systems, the internal coordinates of atoms were fully relaxed until formation energies converge to about 10 meV, and in the case of ordered alloys, the cell shape was also relaxed. The lattice relaxation of our SQS:s do give rise to a small artificial energy induced by the specific magnetic order being fixed in time instead of dynamic.[42] However, these terms are almost fully cancelled in mixing enthalpy calculations as it is present also in our pure CrN calculation as demonstrated by us for the alloy $Cr_{1-x}Al_xN$.[43] Furthermore, the electronic density of states of three $Cr_{1-x}Sc_xN$ solid solution compositions (x = 0.25, 0.50, and 0.75) was calculated for further understanding of electronic properties of the solid solutions. Here, we used fully relaxed supercells from the phase stability study as starting structure. For these electronic densities-of-states (DOS) calculations, the k-point

mesh of $25 \times 25 \times 25$ for binary ScN and $7 \times 7 \times 7$ 128 atoms supercell.

B. Sample preparation

$Cr_{1-x}Sc_xN$ thin films were grown onto one side polished $Al_2O_3(0001)$ substrates using reactive dc magnetron sputtering in a high vacuum chamber with a base pressure of 2×10^{-7} Torr ($\sim 2.7 \times 10^{-5}$ Pa). The chamber is described in detail elsewhere.[44] The 99.95% purity Sc (specified as the ratio of Sc to the amount of rare-earth metals in the target) and 99.99% purity Cr targets have diameters of 75 mm. Prior to deposition, the substrates were cleaned in an ultrasonic bath with trichloroethylene, acetone, and isopropanol for 5 min per step, and subsequently blown dry with N_2. Before deposition, the substrates were heated to the deposition temperature of 600 °C for 1 h to stabilize the temperature and reduce the amount of outgassing during deposition. A series of Cr/Sc magnetron powers of 50/0, 50/40, 50/75, 35/80, 25/85, 15/85, 10/90, and 0/85 W were applied. The substrate was rotating during deposition in order to improve the film uniformity. The depositions were performed in an Ar/N_2 atmosphere with a flow ratio of 40% Ar/60% N_2 resulting in a total gas pressure of $\sim$0.70 Pa. The film thickness of all the samples in this study was kept at 300 nm.

C. Chemical composition analysis

Compositional analysis of as-deposited films was performed by time-of-flight elastic recoil detection analysis (ToF-ERDA). Here, a 36 MeV $^{127}I^{8+}$ beam was directed to the samples at an incident angle of 67.5° with respect to the surface normal, and the target recoils were detected at an angle of 45°. The spectra were analyzed using the CONTES code with the recoil energy of each element converted to a compositional depth profile.[45,46]

D. Structural characterization

Structural characterization of the as-deposited films was performed by X-ray diffraction (XRD) using a Panalytical Empyrean diffractometer with Cu K_α as X-ray source. The θ-2θ scans were measured using a hybrid mirror primary optics in combination with a PIXcel detector in receiving slit mode. For the ω-rocking curves of the $Cr_{1-x}Sc_xN$ 111 peak, the hybrid mirror was used together with a triple axis analyzer as secondary optics for high crystalline quality samples, and a 1/32° fixed slit for low crystalline quality samples. The ϕ-scans were measured using a 2×2 mm crossed slits primary optics and parallel-plate collimator secondary optics. The scans were performed with a steps size of 1° from 0° to 360° with a tilt angle of 54.7° at 2θ angles corresponding to the 200 peaks for the different films.

The transmission electron microscopy (TEM) specimen was prepared by the conventional method: thin film samples were face to face glued and put into a Ti grid, mechanically polished to a thickness of approximately 50 μm, followed by ion milling using a Gatan precision ion polishing system with 5 keV Ar^+ ions until electron transparency, followed by fine polishing using 1.8 keV Ar^+ ions for 30 min and 0.5 keV for 3 h. High resolution transmission electron microscopy (HRTEM), selected area electron diffraction (SAED), and scanning transmission electron microscopy (STEM) were carried out using a FEI Tecnai G2 TF20 UT TEM with a field emission gun operated at 200 kV for a point resolution of 0.19 nm. The microscope is equipped with an energy dispersive X-ray spectroscopy analysis (EDS) system, allowing EDS mapping to be performed in STEM mode.

E. Thermoelectric properties measurements

The in-plane Seebeck coefficient and electrical resistivity of the film were simultaneously measured from room temperature up to $\sim$770 K by an ULVAC-RIKO ZEM3 system at the Technical University of Denmark (DTU) in vacuum with a low pressure helium atmosphere ($\sim$0.09 MPa, purity 99.999% with $<$0.5 ppm residual oxygen). The setup in the ULVAC ZEM3 at DTU was developed for thin films and tested on a series of standard samples of Si-Ge and Bi_2Te_3. The substrate contribution to the Seebeck coefficient and electrical resistivity is negligible, and the instrumental error is within 7%. Temperature-dependent Hall carrier concentration and carrier mobility data were determined on 10 mm $\times$ 10 mm thin film samples by Hall measurements using the IPM-HT Hall-900 K system developed and constructed by Fraunhofer IPM in Freiburg, Germany.

Thermal conductivities of $Cr_{1-x}Sc_xN$ solid solutions were measured at 300 K and 600 K by time-domain thermoreflectance (TDTR). Here, we briefly discuss only the measurements on $Cr_{1-x}Sc_xN$ samples, and readers are referred to Refs. 47 and 48 for details of the TDTR setup and implementation. Before conducting TDTR measurements, the samples were coated with a $\sim$90-nm thick Al film as the transducer for the measurements. In TDTR measurements, laser pulses from an ultrafast laser are split into a pump and a probe beam. The pump beam heats the samples periodically, creating a temperature oscillation in the samples. The probe beam monitors the temperature oscillation at sample surfaces through thermoreflectance (i.e., change of reflectance with temperature). Since the induced temperature oscillation depends on the thermal properties of the samples, TDTR is an accurate approach to measure the thermal conductivity of nanostructures.[49–51] In this study, we used a $1/e^2$ laser radius of 10 μm, a modulation frequency of 10 MHz, and a total laser power of $\sim$40 mW to limit the steady state temperature rise to $<$10 K. The thermal conductivities of $Cr_{1-x}Sc_xN$ were then derived by comparing the TDTR measurements to the calculations of a thermal model.[52] In the analysis, we used the thickness of Al film derived from picosecond acoustics,[53] the heat capacity of CrN and ScN from their bulk values,[54,55] and the heat capacity of $Cr_{1-x}Sc_xN$ alloy films estimated from virtual crystal approximation.

III. RESULTS AND DISCUSSION

A. Theoretical study

Figure 1 shows the calculated mixing enthalpy of the $Cr_{1-x}Sc_xN$ solid solution. The result shows a weak positive asymmetric mixing enthalpy curve for the disordered solid

solution over the entire composition range. The maximum value is 0.061 eV/formula unit (f.u.) at approximately $x = 0.60$. Considering the ordered solid solution of B1-$L1_1$ structure at $x = 0.50$, the result shows a slightly negative mixing enthalpy energy of −0.008 eV/f.u. Here, it should be noted that pure CrN and ScN have rather different lattice constants of 4.128 Å and 4.509 Å, respectively. Thus, if an alloy were to phase-separate coherently, considerable elastic energy penalty terms would also have to be considered. This is in contrast to fully incoherent phase separation that can be modeled directly from the mixing enthalpies of Figure 1. To qualitatively estimate the equilibrium mixing trend at high temperatures, we add the configurational entropy from a mean-field approximation. The contribution of the magnetic entropy to the mixing thermodynamics in the paramagnetic state of the considered alloys is likely to be small. The local magnetic moments of Cr atoms are found to be almost unchanged as a function of alloy composition. The mean of the magnitude of the Cr moments (M) are 2.81 μ_B for CrN, 2.82 μ_B for $Cr_{0.75}Sc_{0.25}N$, 2.84 μ_B for $Cr_{0.50}Sc_{0.50}N$, and 2.85 μ_B for $Cr_{0.25}Sc_{0.75}N$. Thus, the impact of magnetic entropy of Cr atoms, which can be estimated in the paramagnetic state by the formula $S_{MAG} = k_B \times \ln(M+1) \times \text{fraction(Cr)}$, on the alloy phase stability is minimal as it cancels in the derivation of the mixing free energy. At reasonably low temperatures with respect to the melting points of the isostructural alloys, the vibrational contributions are expected to vary rather linearly with composition and thus not influence the mixing thermodynamics significantly. As an example, for the related isostructural B1 $Ti_{1-x}Al_xN$ system, below ~1000 °C, vibrational contributions to the free energy were found to not influence the phase diagram significantly.[56,57]

The results in Figure 1 indicate that while the ordered B1-$L1_1$ phase is stable at low temperatures, there is a tendency for phase separation at temperatures above ~800 °C, once again if we consider incoherent equilibrium phase separation. The miscibility gap is closed by mixing entropy effects at a temperature about 1500 °C, above which a single phase disordered solid solution is stable for all investigated compositions. However, nonequilibrium techniques like magnetron sputtering can induce mixing between CrN and ScN at a growth temperature much lower than the closure of the miscibility gap. This is due to lack of bulk diffusion and since the free energy driving force for either phase separation or ordering is rather small. Furthermore, as-deposited $Cr_{1-x}Sc_xN$ films will remain disordered solid solutions, if strain effects, short range ordering, and vibrational effects are taken into account.

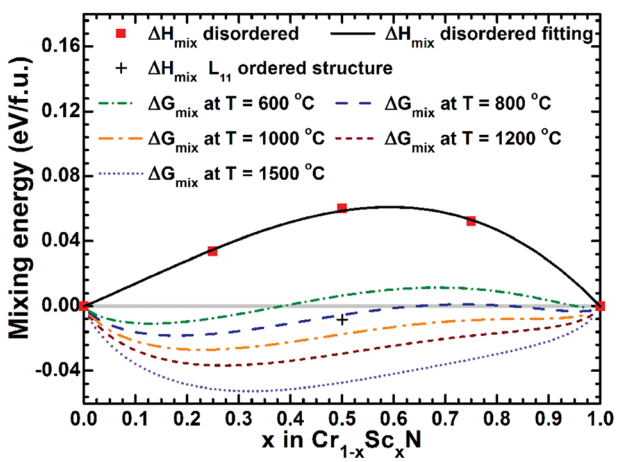

FIG. 1. The calculated mixing enthalpies of substitutionally disordered solid solution, mixing Gibb free energy, and B1-$L1_1$ ordered solid solution of $Cr_{1-x}Sc_xN$, as a function of ScN content.

Our observed result differs from a previous study reported by Zhou *et al.*, who used the generalized gradient approximation (GGA) for the exchange correlation approximation resulting in almost zero mixing enthalpy over the entire composition range in $Cr_{1-x}Sc_xN$ disordered solid solution.[58] The difference observed between these two exchange-correlation approximations can be explained by the following bonding picture: When Sc is added to CrN, the Cr *3d* electrons can delocalize over Sc empty *3d* states resulting in Cr-Sc bonds becoming more favored over the combination of Cr-Cr and Sc-Sc bonds. This electronic effect is counteracted by volume differences that will favor clustering of Cr-rich and Sc-rich regions. Since the GGA and local density approximations (LDA) without Hubbard U-correction favor the delocalization of electrons, they will give strong *d-d* bonds and a large negative contribution to mixing tendency, i.e., lowering the mixing enthalpy. On the other hand, the LDA+U forces the 3d electrons to localize and weaken the *d-d* bonds, thus LDA+U will give a smaller negative contribution to the mixing enthalpy. In both cases, the volume mismatch gives a positive contribution to the mixing enthalpy, in which the GGA calculations are almost exactly balanced with the electronic term. However, in our LDA+U calculations, it is not fully balanced with a resulting net positive mixing enthalpy. Since the LDA+U approximation gives a better description than GGA for pure CrN, it should also give a more trustworthy representation of the mixing enthalpies of CrN-based alloys. The above arguments can also be used to understand the effects of strong electron correlation on the mixing of $Cr_{1-x}Al_xN$,[43] where Al, without *3d* states, breaks Cr-Cr *3d* bonds and the effect of strong electron correlation on mixing is opposite to $Cr_{1-x}Sc_xN$. In $Ti_{1-x}Cr_xN$ where the Ti-Cr *3d* hybridization exists, the observed trend is similar to the present case.[59]

Figure 2(a) shows the electronic density of states (DOS) of $Cr_{1-x}Sc_xN$ solid solutions with $x = 0.25$, 0.50, and 0.75, in comparison with binary CrN and ScN. The underlying bonding physics that give rise to the semiconducting character of ScN and CrN was discussed in Ref. 24 and references therein. In short, in ScN, the three valence electrons from nitrogen plus the three valence electrons from scandium fill the six available states in the bonding band (N *2p* - Sc *3d* e_g + Sc *4s*), while leaving the non-bonding Sc *3d* t_{2g} band empty above the Fermi level. CrN, with three additional electrons also fills half of the non-bonding *3d* t_{2g} state inducing a magnetic splitting. This forms robust local magnetic moments around 3 μ_B and forms a small band gap at the Fermi level.

Pure CrN exhibits a steep slope at the top of the valence band and the bottom of the conduction band. Adding Sc into CrN to form $Cr_{1-x}Sc_xN$ solid solutions resulted in a decrease

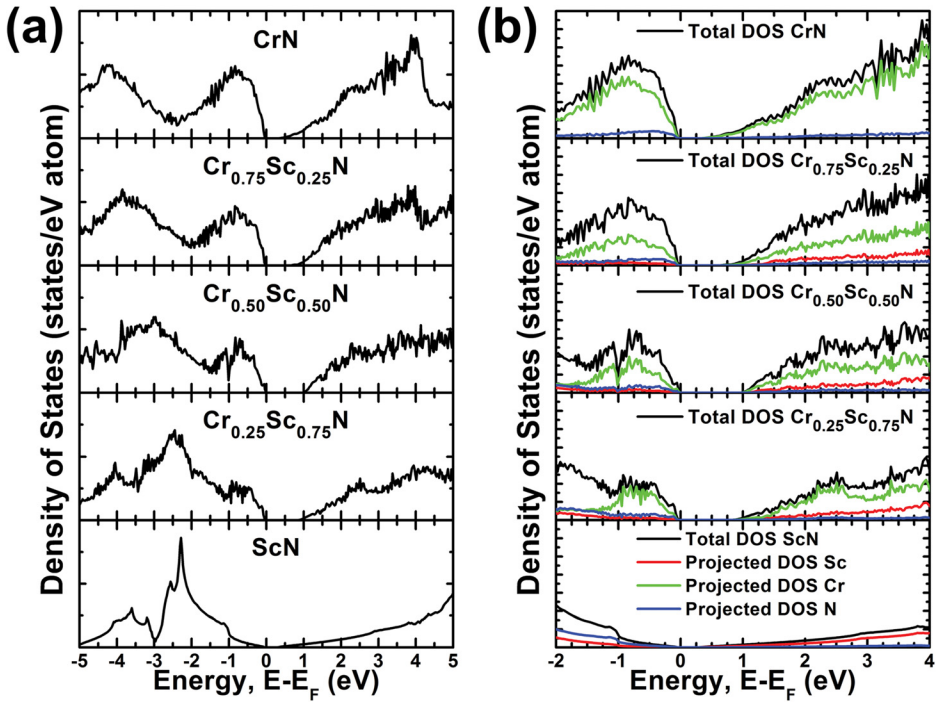

FIG. 2. The calculated electronic density of states (DOS) of $Cr_{1-x}Sc_xN$ solid solution, (a) energy range from −5 to 5 eV which enlarge from the total DOS and (b) the calculated site projected electronic density of states (DOS) of $Cr_{1-x}Sc_xN$ solid solution.

in the states around the top of the valence band and changes the slope on the bottom of the conduction band. In addition, the energy band gap also changes as: CrN 0.20 eV; $Cr_{0.75}Sc_{0.25}N$ 0.80 eV; $Cr_{0.50}Sc_{0.50}N$ 0.90 eV; $Cr_{0.25}Sc_{0.75}N$ 0.60 eV; and ScN 0.20 eV, respectively. While the absolute values of the calculated energy band gap by DFT should be viewed with care, the trend can still be observed. These results indicate that there is a positive bowing parameter for the band gap of this alloy system, with the alloys having larger bandgaps than either of the two pure binaries. The reason behind this positive bowing parameter is the localization of Cr and Sc *d*-states as a result of solid solution disorder. Thus, this localization will reduce the tail of the states at the top of the valence band and the bottom of the conduction band, which results in an increase of the bandgap. This effect is rather small and might have been hidden if the difference between the pure binaries had been larger, since a general linear tread from alloying effect can dominate as the average bond lengths change. Note that this analysis is subject to uncertainty as the DFT (and DFT+U) error of bandgaps might be somewhat different for CrN and ScN.

The projected density of states is shown in Figure 2(b). It indicates that, for the binary CrN, the major states around the top of the valence band and the bottom of the conduction band are given by the occupied t_{2g} states and unoccupied t_{2g} and e_g states, respectively.[23] They are strongly correlated *d* orbitals, resulting in a steep slope in the top of the valence band and the bottom of the conduction band. In contrast, ScN has a moderate slope at the top of the valence band and the bottom of the conduction band. This is due to the fact that, in ScN, the top of the valence band and the bottom of the conduction band are dominated by delocalized *2p* orbitals from N and empty *3d* orbitals from Sc, respectively. Thus, the charge transport in CrN will mostly be *d* to *d* states[24] unlike ScN, where the top of the valence band is dominated by N and Sc contributing to bottom of conduction band, resulting in *p* to *d* states charge transfer. By alloying CrN with Sc, we reduce Cr contribution as well as delocalize the Cr *3d* orbitals with Sc *3d* orbitals, resulting in the states at the top of the valence band decreasing and changing the slope at bottom of conduction band.

In terms of transport properties, there are degrees of delocalization of Cr *3d* orbitals when Sc is added resulting in strong Cr-Sc bonds as compared to Cr-Cr bonds. This delocalization effect should decrease the effective mass of charge carriers resulting in a decreased electrical resistivity in $Cr_{1-x}Sc_xN$ solid solution especially in Cr-rich regime. This delocalization effect also suggests a possibility to improve the Seebeck coefficient of the Sc-rich solid solution and largely retained Seebeck coefficient on the Cr-rich solid solution. To conclude, the theoretical studies of electronic DOS in $Cr_{1-x}Sc_xN$ solid solution support the hypothesis that the thermoelectric properties of ScN and CrN can be altered by forming a solid solution. Note that the charge-carrier-alloy scattering is not considered in this analysis, and can cause an increasing of electrical resistivity and reduction of Seebeck coefficient.

B. Film growth

The compositional analysis with time-of-flight energy recoil detection analysis (ToF-ERDA) of as-deposited $Cr_{1-x}Sc_xN$ solid solution films is shown in Table I. The $Cr_{1-x}Sc_xN$ solid solutions and the CrN film are off-stoichiometric with respect to nitrogen-to-metal ratio by 6–8 at. %. This off-stoichiometry may be due to the combination of a too low N gas flow (60% of total gas flow) during film growth, and the out-diffusion of N from the film around 600 °C. Using the ToF-ERDA results, we obtain ScN molar fractions of x = 0.00, 0.12, 0.24, 0.36, 0.46, 0.60, 0.70, and 1.00. The CrN film contains no impurities within the ToF-ERDA detection limit, which is <0.1 at. % at the present conditions.

TABLE I. Composition of the $Cr_{1-x}Sc_xN$ solid solution films determined by ToF-ERDA. P_{Sc} and P_{Cr} is the applied power on the Sc and Cr targets, respectively.

P_{Cr} [W]	P_{Sc} [W]	Cr [at. %]	Sc [at. %]	N [at. %]	C [at. %]	O [at. %]	F [at. %]
50	0	54.2 ± 1.4	0	45.8 ± 1.5	0	0	0
50	40	48.2 ± 1.4	6.5 ± 0.8	44.3 ± 1.5	0.4 ± 0.2	0.6 ± 0.2	0
50	75	40.2 ± 1.2	12.9 ± 1	44.3 ± 1.5	0.7 ± 0.2	1.5 ± 0.3	0
35	80	34.2 ± 1.1	18.2 ± 1	44.0 ± 1.5	0.7 ± 0.2	2.0 ± 0.3	0.9 ± 0.2
25	85	28.4 ± 1	23.8 ± 0.9	43.3 ± 1.5	0.9 ± 0.2	2.8 ± 0.3	0.8 ± 0.2
15	85	20.5 ± 1	30.5 ± 1.1	44.6 ± 1.5	0.6 ± 0.2	2.9 ± 0.3	0.9 ± 0.2
10	90	15.2 ± 1	35.9 ± 1.2	44.3 ± 1.5	0.4 ± 0.2	3.3 ± 0.4	0.9 ± 0.2
0	85	0	50.3 ± 1.4	43.7 ± 1.5	0.4 ± 0.2	5.0 ± 0.6	0.6 ± 0.2

For the other films, the impurity content (carbon, oxygen, and fluorine) increases with the amount of Sc, and the pure ScN film contain as much as 5 at. % of oxygen. Almost 1 at. % of fluorine is detected in the films with a Sc concentration of more than 18 at. %. The source of the fluorine is most likely from the Sc target, caused by the production process. In addition, Sc also has a high oxygen affinity.[60] Since these films were grown in a high-vacuum system ($\sim 2.7 \times 10^{-5}$ Pa), Sc tends to react with oxygen and carbon in water vapor and carbon dioxide during the deposition, causing the observed increase of the oxygen and carbon impurity levels.

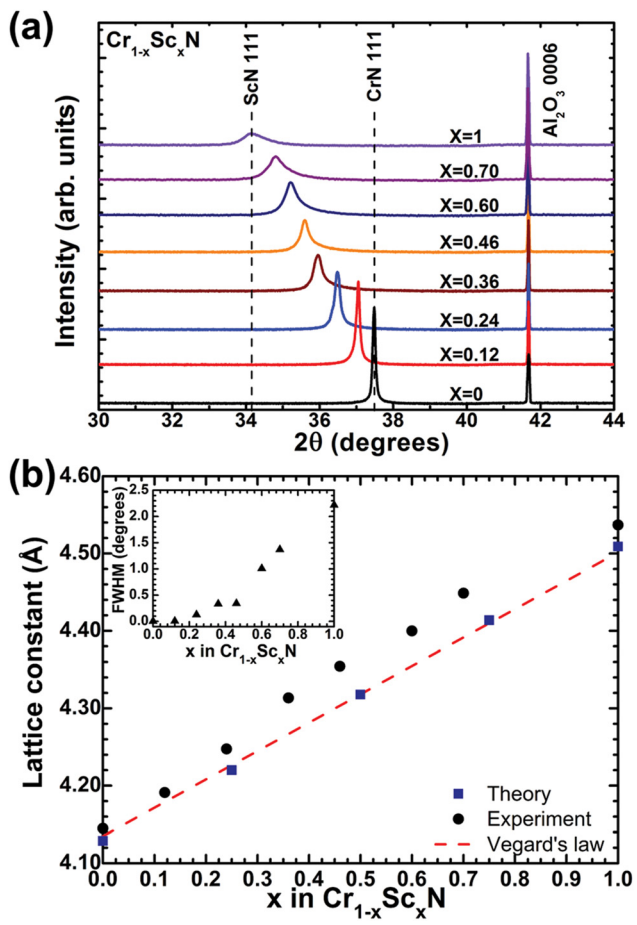

FIG. 3. (a) X-ray diffraction θ-2θ measurements of $Cr_{1-x}Sc_xN$ solid solution thin films on $Al_2O_3(0001)$ and (b) comparison between the calculated and experimentally determined lattice parameters for rocksalt (B1) $Cr_{1-x}Sc_xN$ solid solutions as a function of the Sc content. The purple line indicates Vegard's rule that is obtained from experimentally determined lattice parameters of CrN and ScN from ICDD PDF 01-074-8390 and ICDD PDF 45-097, respectively. Inset shows the Full Width of Half Maxima (FWHM) of as-deposited $Cr_{1-x}Sc_xN$ solid solution films which obtained from ω-scan.

Figure 3(a) shows θ–2θ X-ray diffraction (XRD) patterns from as-deposited $Cr_{1-x}Sc_xN$ solid solution films where x ranges from 0.00 to 1.00. The patterns show the CrN and ScN 111 diffraction peaks at 2θ angles of 37.48° and 34.14°, yielding lattice parameters of 4.145 Å and 4.537 Å, respectively. When alloying CrN with Sc, the CrN 111 peaks are shifted according to the amount of Sc in the film. These results show the formation of $Cr_{1-x}Sc_xN$ solid solutions. The lattice parameters of these solid solution films are calculated and compared to our theoretical results, as shown in Figure 3(b). The calculated and experimentally determined lattice parameters follow the same trend, but the experimental results show larger lattice parameter, because of impurities and to a lesser extent off-stoichiometry.

To confirm the epitaxy, ϕ-scans were performed. Figure 4 shows ϕ-scans of the 200 peaks of CrN, $Cr_{0.54}Sc_{0.46}N$, and ScN in comparison with the $10\bar{1}4$ peak of the Al_2O_3 substrate. All films exhibit six peaks rather than three, as expected for the three-fold cubic symmetry. The additional peaks are due to twin-domain formation caused by two different stacking sequences in the [111]-direction of a face-centered-cubic (fcc) material on Al_2O_3. In addition, there is an in-plane rotation of the domains such that the 200 peaks of the films are located 30° from the $10\bar{1}4$ peaks of the substrate. These results confirm that the films retain the cubic rocksalt structure, and that the epitaxial relationships are

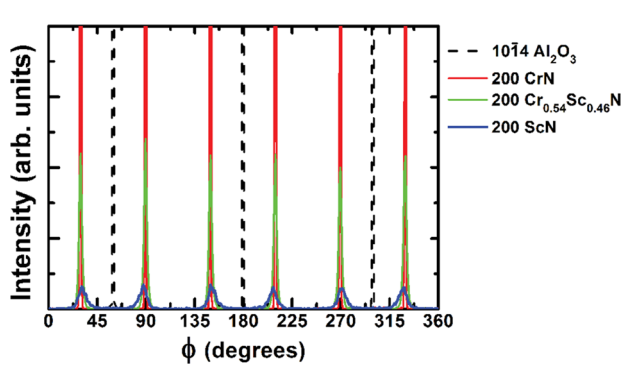

FIG. 4. X-ray diffraction ϕ-scans of (solid lines) the CrN, $Cr_{0.54}Sc_{0.46}N$, and ScN 200 planes, and (dashed lines) the Al_2O_3 $10\bar{1}4$ planes.

$\langle 1\bar{1}0\rangle_f$ //$\langle 10\bar{1}0\rangle_s$ in-plane and $(111)_f$ // $(0001)_s$ out-of-plane, where f = CrN, $Cr_{1-x}Sc_xN$, or ScN, and s = Al_2O_3. Moreover, the fact that CrN peak is narrow and has a high intensity indicates that the CrN is of high crystal quality and well aligned to the Al_2O_3 substrate. The peak intensity decreases when Sc is added to CrN. Moreover, there is a small peak shift of the ScN peaks toward the substrate peaks. This was observed in our previous study[25] and is attributed to the large positive mismatch between the ScN and Al_2O_3 lattices, causing the ScN domains to slightly off-aligned from in-plane epitaxial relationship.

To investigate the crystalline quality of the $Cr_{1-x}Sc_xN$ solid solution films we performed rocking curve measurements and determined the full width at half maximum (FWHM) of the 111 diffraction peaks in Figure 3(a). The full width at half maximum values, presented in Figure 3(b), are increasing with increasing Sc concentration and shows that the crystalline quality is reduced as more Sc is added. This is because of the increased impurity incorporation (of mainly oxygen) and the low mobility of ScN adatoms at the relatively low substrate temperature. Sc has a high affinity to N and is thus likely to form a dimer with N, resulting in a low adatom surface mobility.[61,62] Typically, ScN requires high substrate temperatures (about 800 °C) in order to obtain high crystalline quality films.[25,63] However, in order to be able to compare the thermoelectric properties of the different films, and to prevent decomposition of CrN, the substrate temperature was kept at 600 °C for all depositions.

The microstructure of a selected $Cr_{1-x}Sc_xN$ solid solution film is shown in Fig. 5. The overview cross-section transmission electron microscopy (TEM) of the $Cr_{0.76}Sc_{0.24}N$ solid solution film (Figure 5(a)) reveals that the film consists of columnar domains. The selective area electron diffraction (SAED) pattern with the beam aligned along the [110] zone axis of the film and $[10\bar{1}0]$ zone axis for the Al_2O_3(0001) substrate shows well-defined discrete spots corresponding to an fcc structure epitaxially grown on the substrate, confirming that the film consists of a single phase of high crystalline quality, in agreement with XRD results. The high resolution TEM image of the interface between the $Cr_{0.76}Sc_{0.24}N$ solid solution film and the Al_2O_3 substrate (Figure 5(b)) together with the SAED pattern shows that the film is epitaxial as observed in the ϕ-scan. In addition, scanning transmission electron microscopy (STEM) and energy dispersive X-ray spectroscopy analysis (EDS) mapping (Figure 5(c)) reveals that the film is uniform without any elemental segregation. This confirms that the $Cr_{1-x}Sc_xN$ solid solution films are disordered, as predicted from theory.

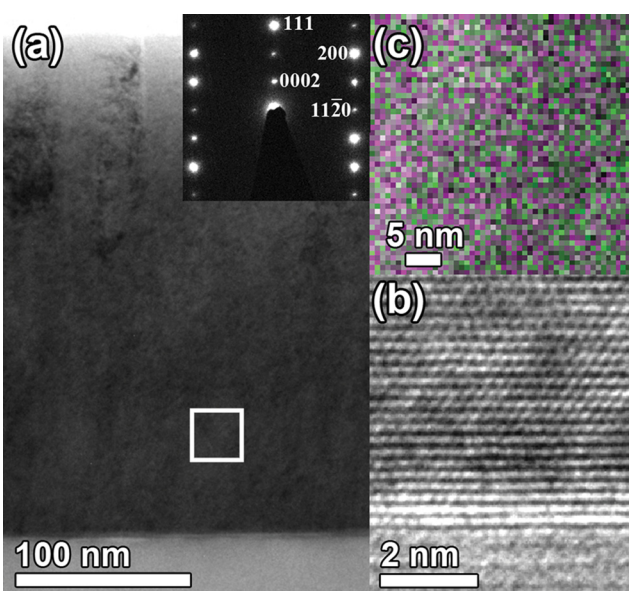

FIG. 5. Cross-section TEM micrographs of $Cr_{0.76}Sc_{0.24}N$ film on Al_2O_3 (a) overview image (inset shows SAED pattern of film and substrate along the [110] and $[10\bar{1}0]$ zone-axes, respectively), (b) interface between film and substrate, and (c) EDS elemental mapping on the area inside the white box with Cr (pink) and Sc (green).

C. Thermoelectric properties

The in-plane electrical resistivity and Seebeck coefficient of the $Cr_{1-x}Sc_xN$ films are shown in Figure 6. CrN shows semiconducting behavior with a resistivity of about ~7 mΩcm at room temperature which is slowly decreasing with temperature to 2.5 mΩcm at 770 K since CrN becomes unstable above this temperature, as shown in Figure 6(a). This resistivity range is quite low for CrN as compared to

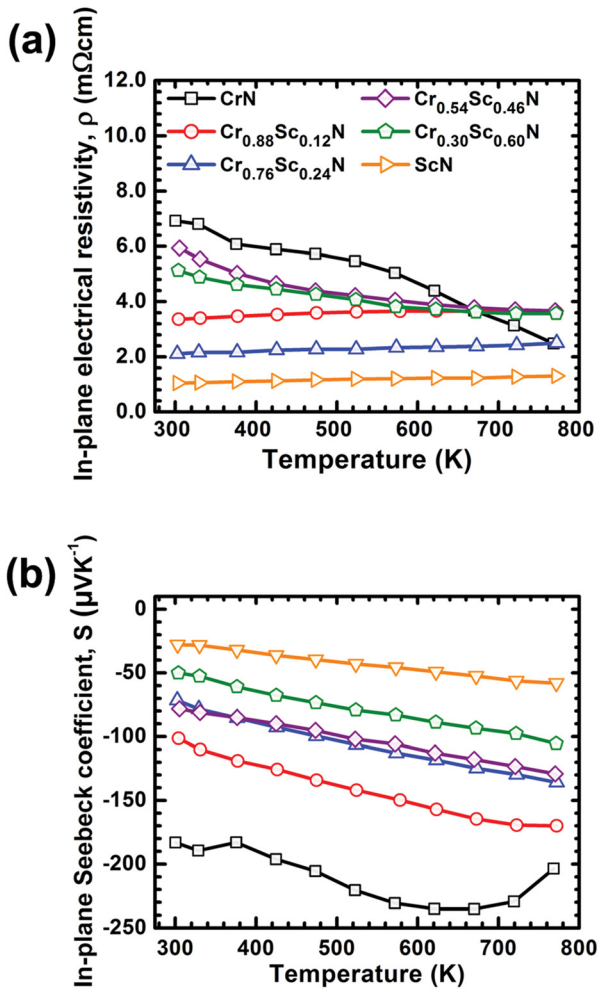

FIG. 6. The measured in-plane thermoelectric properties of $Cr_{1-x}Sc_xN$ solid solution films (a) electrical resistivity and (b) Seebeck coefficient.

reported literature values.[4,14,18–21] Hall measurements (see supplementary material) were performed on all films. These yielded a carrier concentration of $2.3 \times 10^{19}\,cm^{-3}$ for CrN at room temperature, increasing non-linearly to $7.4 \times 10^{19}\,cm^{-3}$ at 675 K, with a corresponding decrease in carrier mobility from 33 to 20.5 $cm^2\ V^{-1}\ s^{-1}$, which can be attributed to vacancy scattering. Based on these results, it can be concluded that the low resistivity in our CrN films is due to a high electron concentration which is thermally activated from N vacancies.[21,64] This is a different mechanism than that reported recently for stoichiometric CrN,[65] where it was shown that the resistivity of CrN can be reduced by improving the crystal quality by annealing to stoichiometry, and thereby yielding an increase in carrier mobility.

Figure 6(b) shows the Seebeck coefficients of all $Cr_{1-x}Sc_xN$ films ($0 \le x \le 1$). CrN exhibits a negative Seebeck coefficient of $-183\,\mu VK^{-1}$ at room temperature and $-203\,\mu V\,K^{-1}$ at 770 K. The negative Seebeck coefficient indicates that electrons are the majority charge carriers in CrN, which is confirmed by the Hall measurements (supplementary material). In addition, our CrN films shows a large Seebeck coefficient especially from room temperature to 675 K compared to reported literature values.[18–20,65,66] This can be explained by the influence of N defects on the electronic structure of CrN. As pointed out by Mozafari *et al.*[64] that N vacancies can increase the slope of electronic density of states (DOS) around Fermi level, which in turn can increase the Seebeck coefficient according to the Mott equation.[67,68] This large Seebeck coefficient and low resistivity in the CrN film yields a relatively high thermoelectric power factor of $\sim 1.7 \times 10^{-3}\,W\,m^{-1}\,K^{-2}$ at 720 K, as seen in Figure 7, which is similar to what has been observed for Na-doped PbTe.[69]

The present ScN films exhibits electrical resistivity of 1.0 mΩcm at room temperature, increasing to 1.4 mΩcm at 770 K. This is a rather high resistivity compared to previous reports,[25,26] but still follows the same trend as a metallic-like conduction. The reason for the high resistivity in this ScN sample is most likely because of the higher O impurity content. Furthermore, the ScN film exhibits Seebeck coefficients decreasing from $-27.9\,\mu V/K$ at room temperature to $-58.1\,\mu V/K$ at 770 K; all those are lower than those reported in Refs. 25 and 26 as a result of the O impurities. Thus, the thermoelectric power factor is also lower.

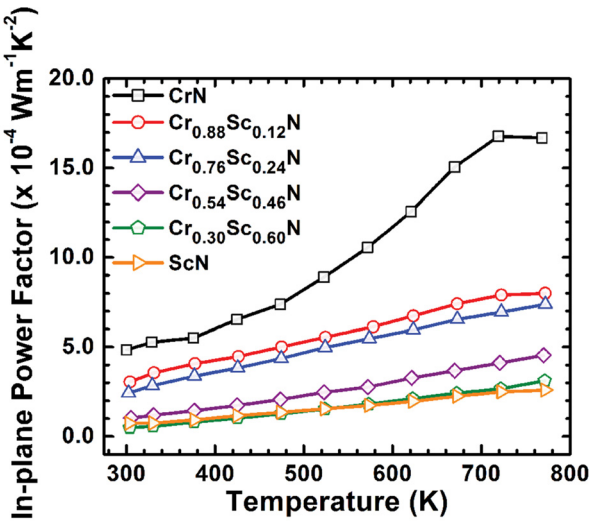

FIG. 7. The calculated in-plane thermoelectric power factor from measured electrical resistivity and Seebeck coefficient of $Cr_{1-x}Sc_xN$ solid solution films.

As for the thermoelectric properties of $Cr_{1-x}Sc_xN$ solid solution films, the results show that the electrical resistivity at a given temperature tends to decrease with increasing Sc content (Figure 6(a)). The effect is more substantial in the low temperature region for $T < 600\,°C$. At first, $Cr_{0.88}Sc_{0.12}N$ and $Cr_{0.76}Sc_{0.24}N$ have resistivity of 3.4 mΩcm and 2.1 mΩcm, respectively, at room temperature. Then, their conduction behavior changes from semiconducting to metallic-like conduction, and as a result, their resistivity linearly increases to 3.6 mΩcm and 2.5 mΩcm at 770 K, respectively. Further increasing the Sc content in $Cr_{1-x}Sc_xN$ solid solution, however, leads to an increase in resistivity, especially at the Sc-rich sample where resistivity should show a similarity with ScN, as we expected due to theoretical results suggest that the delocalization effect from empty *3d* state in Sc should improve the carrier mobility. However, Hall measurements (supplementary material) results show that the reason of change in electrical resistivity after alloying is an increase of charge carrier concentration instead of increasing carrier mobility (see Figure S3(a) in supplementary material), which is contrary to our theoretical suggestion. This is because of the amount of O impurities acting as dopants and increasing with Sc content (see Table I or Figure S1 in supplementary material). These impurities lead to an electron-alloy scattering increasing electrical resistivity. Moreover, there is also a possibility that a secondary phase of Sc_2O_3 can form at grain or domain boundaries apart from electron-alloy scattering.

All $Cr_{1-x}Sc_xN$ solid solution films show a linear temperature dependence of the negative Seebeck coefficient. The linearly temperature dependent negative Seebeck coefficient for the solid solutions suggest that all samples are degenerate semiconductors with electrons as majority carrier which is confirmed by Hall measurement (see supplementary material). With increasing Sc concentration in $Cr_{1-x}Sc_xN$ solid solution, the Seebeck coefficient decreases over the whole measured temperature range. This is due to two reasons: (i) the delocalization of *3d* electrons of Cr over Sc *3d* orbitals leading to a reduction of Seebeck coefficient; (ii) the O impurities leading to an increasing electron concentration according to Hall measurement results (see supplementary material). In contrast, there is an increase of the Seebeck coefficient for the Sc-rich samples compared to ScN, i.e., $Cr_{0.30}Sc_{0.60}N$ has a Seebeck coefficient of $-105.5\,\mu V\,K^{-1}$ compare to $-58.1\,\mu V\,K^{-1}$ at 770 K for ScN. This supports the explanation that the localized *3d* orbital of Cr can improve Seebeck coefficient of ScN by increasing of the slope around Fermi level in the ScN electronic density of states. Thus, Sc-rich solid solution films show an improvement in thermoelectric power factor (Figure 7) compared to pure ScN. Reducing the amount of O impurities (noting that the present work was performed at high-vacuum conditions instead of ultrahigh vacuum as in previous works[25,26]) can thus be expected to improve the thermoelectric properties of

$Cr_{1-x}Sc_xN$ solid solution films, in line with our theoretical predictions.

Figure 8 shows the thermal conductivity of selected $Cr_{1-x}Sc_xN$ ($0 \le x \le 1$) samples. At 300 K, the measured thermal conductivity κ of ScN is 11.0 ± 1 W m^{-1} K^{-1}, similar to prior TDTR measurements on a sputterred, 306-nm thick ScN thin film.[16] The measured thermal conductivity κ of CrN is 3.50 ± 0.3 W m^{-1} K^{-1}, which is larger than previously reported κ of nearly stoichiometric bulk CrN[18,19] (1.76 W m^{-1} K^{-1} and 1.65 W m^{-1} K^{-1} for samples with a grain size of 400 ± 100 nm and ~13 nm, respectively) and κ of oxygen-free CrN ceramics[20] (1.35–2.28 W m^{-1} K^{-1} for samples with a grain size of ~200 nm and a density only 56%–66% of the density of fully condensed CrN). Since prior CrN samples were not fully dense due to voids that are inevitably formed during sintering[70] of bulk CrN[18,19] and CrN ceramics,[20] the prior reported κ of CrN is significantly reduced and limited by the level of voids.

By alloying CrN with ScN, we find that the thermal conductivity of $Cr_{1-x}Sc_xN$ solid solutions at 300 K are 2.70 ± 0.2 W m^{-1} K^{-1} and 2.30 ± 0.2 W m^{-1} K^{-1} for $Cr_{0.88}Sc_{0.12}N$ and $Cr_{0.54}Sc_{0.46}N$, respectively, as a result of phonon-alloy scattering. At 600 K, the thermal conductivity of CrN, $Cr_{1-x}Sc_xN$ solid solutions with $x = 0.12$ and $x = 0.46$, and ScN are 4.20 ± 0.3 W m^{-1} K^{-1}, 3.70 ± 0.3 W m^{-1} K^{-1}, 3.1 ± 0.2 W m^{-1} K^{-1}, and 12.2 ± 1 W m^{-1} K^{-1}, respectively. This is due to the increase of lattice thermal conductivity κ_{ph} from heat capacity, as well as the increase of electronic thermal conductivity κ_{el} by temperature rise (~0.2–0.3 W m^{-1} K^{-1}).

According to the power factor and thermal conductivity results, we can estimate the thermoelectric figure of merit (ZT) of CrN as ~0.2 and 0.10 and 0.06 for $Cr_{0.88}Sc_{0.12}N$ and $Cr_{0.54}Sc_{0.46}N$, respectively. These numbers should only be considered estimates since the measurements are performed in different orientations (S and σ are measured in-plane, while κ is measured out-of-plane). Even for cubic materials, there will be anisotropy effects in highly oriented (in this case, epitaxial) films.

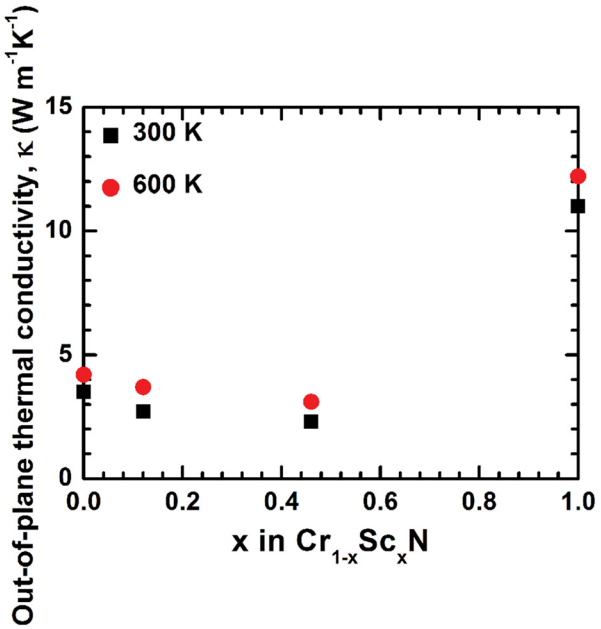

FIG. 8. Measured out-of-plane thermal conductivity κ of selected $Cr_{1-x}Sc_xN$ films at 300 K (squares) and 600 K (circles). The measurement uncertainties are indicated in the main text.

The expected substantial reduction in thermal conductivity due to alloy scattering of phonons is observed for the solid solutions. The ZT of solid solution samples is, however, not improved because of the cancellation between thermal conductivity and electrical conductivity. For the sample $Cr_{0.54}Sc_{0.46}N$ which has the lowest κ, the thermal conductivity increased by 35% from 300 K to 600 K. Thus, although the electrical conductivity also increased by 35%, high temperature (e.g., 600 K) does not increase ZT.

IV. CONCLUSIONS

We have used density functional theory calculations to determine the phase stability of $Cr_{1-x}Sc_xN$ solid solutions for thermoelectric applications. Our results predict that if strain and short-range ordering are considered, the $Cr_{1-x}Sc_xN$ is thermodynamically stable in disordered B1 solid solutions at $T = 800$ °C rather than in the B1-$L1_1$ ordered solid solutions stable at 0 K. The electronic density of states of disordered $Cr_{1-x}Sc_xN$ solid solutions indicate a possibility of improvement of power factor due to empty Sc *3d* orbital available for delocalization of Cr *3d* electrons giving a decreasing electrical resistivity with retained Seebeck coefficient in the Cr-rich regime. On the other hand, the Cr *3d* still dominate in conduction in the Sc-rich regime. This causes an increase of the Seebeck coefficient for ScN.

$Cr_{1-x}Sc_xN$ thin films were grown on $Al_2O_3(0001)$. Structural and chemical composition analyses confirm the formation of disordered solid solutions as theoretically predicted. For thermoelectric properties, CrN exhibits a maximum power factor of 1.7×10^{-3} W m^{-1} K^{-2} at 720 K, as a result of a high electron concentration thermally activated from N vacancies. In terms of thermoelectric properties of $Cr_{1-x}Sc_xN$ solid solution thin films, an increase in the absolute value of the Seebeck coefficient is observed for Sc-rich solid solutions as compared to ScN, despite a relatively high amount of O impurities, indicating prospects for further improvements.

SUPPLEMENTARY MATERIAL

See supplementary material for the oxygen incorporation trend and Hall measurement of the $Cr_{1-x}Sc_xN$ thin films, where $0 \le x \le 1$.

ACKNOWLEDGMENTS

The research leading to these results has received funding from the European Research Council under the European Community's Seventh Framework Programme (FP/2007-2013)/ERC Grant Agreement No. 335383, the Swedish Research Council (VR) through Project Grants No. 621-2012-4430, 621-2011-4417, and 330-2014-6336, and the Marie Sklodowska Curie Actions, Cofund Project INCA 60098, the Linnaeus Strong Research Environment LiLi-

NFM, the Swedish Government Strategic Research Area in Materials Science on Functional Materials at Linköping University (Faculty Grant SFO-Mat-LiU No. 2009-00971), and the Swedish Foundation for Strategic Research through the Future Research Leaders 5 Program. The calculations were performed using computer resources provided by the Swedish national infrastructure for computing (SNIC) at the National Supercomputer Centre (NSC). N.V.N. would like to thank the financial support from the NanoCaTe project (FP7-NMP No. 604647). B.S. and Y.K.K. acknowledge the National University of Singapore Startup Grant.

[1]T. M. Tritt, Annu. Rev. Mater. Res. **41**, 433 (2011).
[2]A. Shakouri, Annu. Rev. Mater. Res. **41**, 399 (2011).
[3]L. E. Toth, *Transition Metal Carbies and Nitrides* (Academic Press, New York/London, 1971).
[4]D. Gall, C.-S. Shin, T. Spila, M. Odén, M. J. H. Senna, J. E. Greene, and I. Petrov, J. Appl. Phys. **91**, 3589 (2002).
[5]J. Lin, N. Zhang, W. D. Sproul, and J. J. Moore, Surf. Coat. Technol. **206**, 3283 (2012).
[6]J. Lin, W. D. Sproul, and J. J. Moore, Surf. Coat. Technol. **206**, 2474 (2012).
[7]C. Lorenzo-Martin, O. Ajayi, A. Erdemir, G. R. Fenske, and R. Wei, Wear **302**, 963 (2013).
[8]P. Eklund, S. Kerdsongpanya, and B. Alling, J. Mater. Chem. C **4**, 3905 (2016).
[9]M. Chen, S. Wang, J. Zhang, D. He, and Y. Zhao, Chem.—Eur. J. **18**, 15459 (2012).
[10]S. Wang, X. Yu, J. Zhang, M. Chen, J. Zhu, L. Wang, D. He, Z. Lin, R. Zhang, K. Leinenweber, and Y. Zhao, Phys. Rev. B **86**, 064111 (2012).
[11]P. Subramanya Herle, M. S. Hegde, N. Y. Vasathacharya, S. Philip, M. V. Rama Rao, and T. Sripathi, J. Solid State Chem. **134**, 120 (1997).
[12]J. Lin, W. D. Sproul, and J. J. Moore, Mater. Lett. **89**, 55 (2012).
[13]C. Petrogalli, L. Montesano, M. Gelfi, G. M. La Vecchia, and L. Solazzi, Surf. Coat. Technol. **258**, 878 (2014).
[14]C. Constantin, M. B. Haider, D. Ingram, and A. R. Smith, Appl. Phys. Lett. **85**, 6371 (2004).
[15]D. Gall, I. Petrov, N. Hellgren, L. Hultman, J. E. Sundgren, and J. E. Greene, J. Appl. Phys. **84**, 6034 (1998).
[16]V. Rawat, Y. K. Koh, D. G. Cahill, and T. D. Sands, J. Appl. Phys. **105**, 024909 (2009).
[17]S. W. King, R. F. Davis, and R. J. Nemanich, J. Vac. Sci. Technol. A **32**, 061504 (2014).
[18]C. X. Quintela, F. Rivadulla, and J. Rivas, Appl. Phys. Lett. **94**, 152103 (2009).
[19]C. X. Quintela, B. Rodríguez-González, and F. Rivadulla, Appl. Phys. Lett. **104**, 022103 (2014).
[20]O. Jankovský, D. Sedmidubský, Š. Huber, P. Šimek, and Z. Sofer, J. Eur. Ceram. Soc. **34**, 4131 (2014).
[21]X. Y. Zhang, J. S. Chawla, B. M. Howe, and D. Gall, Phys. Rev. B **83**, 165205 (2011).
[22]D. Gall, C.-S. Shin, R. T. Haasch, I. Petrov, and J. E. Greene, J. Appl. Phys. **91**, 5882 (2002).
[23]A. Herwadkar and W. R. L. Lambrecht, Phys. Rev. B **79**, 035125 (2009).
[24]A. S. Botana, F. Tran, V. Pardo, D. Baldomir, and P. Blaha, Phys. Rev. B **85**, 235118 (2012).
[25]S. Kerdsongpanya, N. Van Nong, N. Pryds, A. Zukauskaite, J. Jensen, J. Birch, J. Lu, L. Hultman, G. Wingqvist, and P. Eklund, Appl. Phys. Lett. **99**, 232113 (2011).
[26]P. V. Burmistrova, J. Maassen, T. Favaloro, B. Saha, S. Salamat, Y. R. Koh, M. S. Lundstrom, A. Shakouri, and T. D. Sands, J. Appl. Phys. **113**, 153704 (2013).
[27]S. Kerdsongpanya, B. Alling, and P. Eklund, Phys. Rev. B **86**, 195140 (2012).
[28]S. Kerdsongpanya, B. Alling, and P. Eklund, J. Appl. Phys. **114**, 073512 (2013).
[29]W. Kohn and L. J. Sham, Phys. Rev. **140**, A1133 (1965).
[30]P. E. Blöchl, Phys. Rev. B **50**, 17953 (1994).
[31]G. Kresse and J. Furthmüller, Phys. Rev. B **54**, 11169 (1996).
[32]G. Kresse and D. Joubert, Phys. Rev. B **59**, 1758 (1999).
[33]V. I. Anisimov, J. Zaanen, and O. K. Andersen, Phys. Rev. B **44**, 943 (1991).
[34]S. L. Dudarev, G. A. Botton, S. Y. Savrasov, C. J. Humphreys, and A. P. Sutton, Phys. Rev. B **57**, 1505 (1998).
[35]B. Alling, T. Marten, and I. A. Abrikosov, Phys. Rev. B **82**, 184430 (2010).
[36]A. Zunger, S. H. Wei, L. G. Ferreira, and J. E. Bernard, Phys. Rev. Lett. **65**, 353 (1990).
[37]A. V. Ruban and I. A. Abrikosov, Rep. Prog. Phys. **71**, 046501 (2008).
[38]B. Alling, A. V. Ruban, A. Karimi, O. E. Peil, S. I. Simak, L. Hultman, and I. A. Abrikosov, Phys. Rev. B **75**, 045123 (2007).
[39]B. Alling, Phys. Rev. B **89**, 085112 (2014).
[40]B. Alling, C. Höglund, R. Hall-Wilton, and L. Hultman, Appl. Phys. Lett. **98**, 241911 (2011).
[41]H. J. Monkhorst and J. D. Pack, Phys. Rev. B **13**, 5188 (1976).
[42]P. Steneteg, B. Alling, and I. A. Abrikosov, Phys. Rev. B **85**, 144404 (2012).
[43]B. Alling, L. Hultberg, L. Hultman, and I. A. Abrikosov, Appl. Phys. Lett. **102**, 031910 (2013).
[44]F. Eriksson, G. A. Johansson, H. M. Hertz, and J. Birch, Opt. Eng. **41**, 2903 (2002).
[45]M. S. Janson, *CONTES, Conversion of Time-Energy Spectra, a Program for ERDA Data Analysis* (Uppsala University, 2004).
[46]J. Jensen, D. Martin, A. Surpi, and T. Kubart, Nucl. Instrum. Methods B **268**, 1893 (2010).
[47]B. Sun and Y. K. Koh, Rev. Sci. Instrum. **87**, 064901 (2016).
[48]P. Jiang, B. Huang, and Y. K. Koh, Rev. Sci. Instrum. **87**, 075101 (2016).
[49]B. Huang and Y. K. Koh, Carbon **105**, 268 (2016).
[50]E. Ziade, J. Yang, G. Brummer, D. Nothern, T. Moustakas, and A. J. Schmidt, Appl. Phys. Lett. **107**, 091605 (2015).
[51]H. Zhang, X. Chen, Y.-D. Jho, and A. J. Minnich, Nano Lett. **16**, 1643 (2016).
[52]D. G. Cahill, Rev. Sci. Instrum. **75**, 5119 (2004).
[53]C. Thomsen, H. T. Grahn, H. J. Maris, and J. Tauc, Phys. Rev. B **34**, 4129 (1986).
[54]J. P. De Luca and J. M. Leitnaker, J. Am. Ceram. Soc. **56**, 126 (1973).
[55]B. Saha, J. Acharya, T. D. Sands, and U. V. Waghmare, J. Appl. Phys. **107**, 033715 (2010).
[56]A. Wang, S.-L. Shang, Y. Du, L. Chen, J. Wang, and Z.-K. Liu, J. Mater. Sci. **47**, 7621 (2012).
[57]N. Shulumba, O. Hellman, Z. Raza, B. R. Alling, J. Barrirero, F. Mücklich, I. A. Abrikosov, and M. Odén, "Lattice vibrations change the solid solubility of an alloy at high temperatures," Phys. Rev. Lett. **117**, 205502 (2016).
[58]L. Zhou, D. Holec, and P. H. Mayrhofer, J. Phys. D: Appl. Phys. **46**, 365301 (2013).
[59]B. Alling, Phys. Rev. B **82**, 054408 (2010).
[60]M. A. Moram, Z. H. Barber, and C. J. Humphreys, Thin Solid Films **516**, 8569 (2008).
[61]H. A. H. Al-Brithen, A. R. Smith, and D. Gall, Phys. Rev. B **70**, 045303 (2004).
[62]H. A. H. Al-Brithen, E. M. Trifan, D. C. Ingram, A. R. Smith, and D. Gall, J. Cryst. Growth **242**, 345 (2002).
[63]P. V. Burmistrova, D. N. Zakharov, T. Favaloro, A. Mohammed, E. A. Stach, A. Shakouri, and T. D. Sands, J. Mater. Res. **30**, 626 (2015).
[64]E. Mozafari, B. Alling, P. Steneteg, and I. A. Abrikosov, Phys. Rev. B **91**, 094101 (2015).
[65]C. X. Quintela, J. P. Podkaminer, M. N. Luckyanova, T. R. Paudel, E. L. Thies, D. A. Hillsberry, D. A. Tenne, E. Y. Tsymbal, G. Chen, C.-B. Eom, and F. Rivadulla, Adv. Mater. **27**, 3032 (2015).
[66]P. Tomeš, D. Logvinovich, J. Hejtmánek, M. H. Aguirre, and A. Weidenkaff, Acta. Mater. **59**, 1134 (2011).
[67]N. F. Mott and H. Jones, *The Theory of the Properties of Metals and Alloys* (Dover Publications, Inc., New York, 1958).
[68]J. P. Heremans, V. Jovovic, E. S. Toberer, A. Saramat, K. Kurosaki, A. Charoenphakdee, S. Yamanaka, and G. J. Snyder, Science **321**, 554 (2008).
[69]J. R. Sootsman, H. Kong, C. Uher, J. J. D'Angelo, C.-I. Wu, T. P. Hogan, T. Caillat, and M. G. Kanatzidis, Angew. Chem. Int. Ed. **47**, 8618 (2008).
[70]L. C. De Jonghe and M. N. Rahaman, in *Handbook of Advanced Ceramics*, edited by F. Aldinger, N. Claussen, R. M. Spriggs, K. Uchino, K. Koumoto, and M. Kaneno (Academic Press, Oxford, 2003), p. 187.